Computational investigation of cavity flow control using a passive device

B. Khanal
bidur.khanal@eng.ox.ac.uk
Department of Engineering Science
University of Oxford
Oxford, UK

K. Knowles
k.knowles@cranfield.ac.uk
Aeromechanical Systems Group
Cranfield University
Shrivenham, UK

A. J. Saddington
a.j.saddington@cranfield.ac.uk

ABSTRACT

In this paper, flow control effectiveness of a passive device in relation to open cavity flowfield is investigated computationally and compared with experimental work. Specifically the modification in the cavity flowfield due to the presence of a spoiler is studied in details to explain the physics behind the flow control effects. A combination of 2D and 3D flow visualisation tools are used to understand the flow behaviour inside the cavity and the quantitative analysis of the unsteady pressure fluctuations is also performed to assess the unsteady effects. Flow simulations with a turbulence model based on a hybrid RANS/LES (commonly known as Detached-Eddy Simulation (DES)) are used in this study. The time-mean flow visualisation clearly showed the presence of three dimensional effects inside the empty cavity whereas the 3D effects were found to diminish in the presence of a spoiler. In the unsteady flow analysis, near-field acoustic spectra were computed for empty cavity as well as cavity-with-spoiler cases. Study of unsteady pressure spectra for the cavity-with-spoiler case was found to record the complete suppression of the dominant tones in the presence of the spoiler. The analysis has indicated that the main reason behind this suppression is due to the inability of faintly energised vortical structures (faintly energised as a result of the extraction of turbulent kinetic energy by the spoiler) to maintain the unsteady flapping of the separated shear layer.

Paper No. 3667. Manuscript received 18 November 2010, revised version received 6 June 2011, accepted 28 June 2011.

https://doi.org/10.1017/S0001924000006679 Published online by Cambridge University Press

NOMENCLATURE

2D	two-dimensional
3D	three-dimensional
CFD	computational fluid dynamics
C_p	pressure coefficient
D	cavity depth, m
f_n	frequency of the nth mode, Hz
K	ratio of the velocity in the shear layer to the freestream velocity
L	cavity length, m
LIC	line integral convolution
M_∞	flow Mach number
n	cavity oscillation mode number
St	Strouhal number, St = $f D/U_\infty$
U_∞	freestream velocity, ms^{-1}
W	cavity width, m
x, y, z	cartesian co-ordinate system, origin at the top left corner of the upstream wall
α	an empirical constant, $\alpha = 0{\cdot}062(L/D)$
δ	boundary-layer thickness at a velocity of $0{\cdot}99U_\infty$, m
ρ	fluid density, kg/m^3
γ	ratio of specific heats of test fluid ($\gamma = 1{\cdot}4$ for air)

1.0 INTRODUCTION

Cavity geometries are frequently encountered in aerospace applications, such as wheel wells, weapons bays, and other fuselage openings and are also widely known to be the major contributor of aerodynamic noise. Unsteady flow approaching a simple cavity geometry produces complex features consisting of flow-induced resonant tones, multiple flow and acoustic instabilities, and wave interactions. Cavities do also have some benefits, particularly, the internal weapons bays on military aircraft have several design advantages. Reduced aerodynamic drag, low radar cross-section and avoidance of aerodynamic heating of the store are a few examples of these. However, once the weapons bay doors are opened, the flowfield is dependent on the cavity geometry and the freestream flow conditions. The resultant unsteady flowfield undergoes interaction with the stores at the beginning of the store release leading to several undesirable aerodynamic effects. The self-sustaining pressure fluctuations in the cavity can cause cavity resonance which in turn leads to structural fatigue of the aircraft and the store. In addition, the interaction of the store with the unsteady shear layer formed over the cavity can lead to unpredicted motion of the store. Hence, a study of cavity flowfield is necessary to understand the flow physics responsible for these phenomena and to propose a suitable methods to control them.

Numerous studies[1,2,3] have been carried out to understand complex flow features existing in cavities and many more[4,5,6] are continuing to understand the cause behind such complex flowfields and suppressing the resonant tones. Although initially the suppressing technique might seem simple enough such that any scheme that disrupts the resonance mechanism can be used to suppress resonant tones, finding a practical solution is not straightforward. There are currently three main approaches which are being used to vary the way the flow behaves in the cavity. They are: passive, active open-loop, and closed-loop flow controls. Passive methods involve manipulating the cavity geometry by either modifying the cavity walls slanting angle or adding

https://doi.org/10.1017/S0001924000006679 Published online by Cambridge University Press

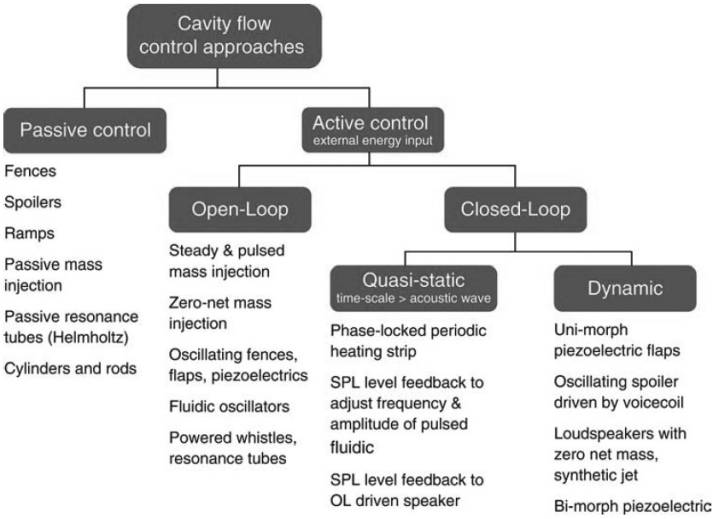


Figure 1. Classification of flow control methods, from Ref. 8.

mechanical devices to deliberately alter the flow inside the cavity. The other two methods involve manipulating the flow inside the cavity by devices that require external energy input e.g. jets or oscillating flaps. They can be either of the open or closed-loop types. Closed-loop control requires the implementation of a feedback loop in the control system allowing it to continuously monitor and update the control parameters to match the changing flow conditions. Hence, closed-loop control systems are more suitable for time-varying and off-design situations. The closed loop system developed (see Ref. 7) to suppress the resonant modes from a weapons-bay was not very successful although this was blamed on the poor performance of the actuators. Active open-loop methods have been found to be limited by actuator bandwidth, and they require large actuator power to be effective[7] whereas closed-loop techniques introduce greater complexity and are not mature enough yet. At this point, it is important to point out that passive and active open-loop schemes break the resonance cycle in a fundamentally different way to the closed-loop counterparts. Because the dynamics of a linear system cannot be changed with open-loop control, any open-loop method used to modify the cavity resonance cycles must do so at finite amplitudes, typically at amplitudes comparable to the tones being suppressed. By contrast, closed-loop control can act by changing the dynamics of the linear system, which implies that low-power actuators can be used effectively. A classification of various flow control scheme is depicted in Fig. 1[8]. In this work, computational study of empty cavity and cavity in presence of passive devices (spoiler in this case) are performed using a turbulence model based on one-equation DES formulation[9].

With regards to the choice of turbulence model selected in this simulation, it is necessary to highlight the limitations of Reynolds-averaged Navier-Stokes (RANS) solver. Several computational studies in the past have experienced a common limitation with RANS solver and turbulence models applied to unsteady flows[9,10,11]. The RANS solver produces increased eddy viscosity which causes excessive damping of the unsteadiness of the flowfield. Spatially filtered models such as Large-Eddy Simulation (LES) have provided improved results for simulating unsteady flows. LES models, however, are currently limited to low Reynolds numbers because of the computing resources required to resolve the small-scale turbulent structures. LES is not

https://doi.org/10.1017/S0001924000006679 Published online by Cambridge University Press

yet, therefore, a feasible tool for the simulation of cavity flowfields at transonic speeds. Recently, hybrid methods which behave as a standard RANS model within the attached boundary layer and as a LES Sub-Grid Scale model in the rest of the flow (more commonly known as DES) have been introduced to address this problem[9,12,13]. A hybrid RANS/LES model[9] was, therefore, chosen for this study.

Cavity flows are usually classified by the length-to-depth ratio (L/D) of the cavity and four different types of cavity flows are found to be present depending on the value of this ratio. The experimental study of Stallings and Wilcox[14] in the 1980s led to the classification of the cavity flow types. Schematics representing all four cavity flow types and corresponding floor pressure distributions are shown in Fig. 2.

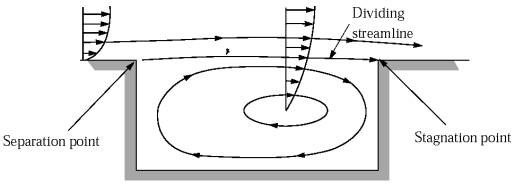
Cavity flows exhibit a wide variety of phenomena whose precise nature depends sensitively on a number of parameters including the value of L/D. Tracy and Plentovich[16] investigated the variations in the values of L/D and concluded that the dependence of the cavity flow type on Mach number in addition to L/D. The other important parameters that affect cavity flow types are incoming boundary-layer thickness (δ), ambient density (ρ), viscosity (μ), and speed of sound (a_0). Although the underlying physical mechanisms vary, it is known that self-sustaining oscillations develop over a wide range of these parameters. In compressible flows, cavity oscillations are typically described as a flow-acoustic resonance mechanism. This mechanism may be summarised as follows: small instabilities in the shear layer interact with the downstream edge of the cavity and generate acoustic waves. These acoustic waves propagate upstream to the region near shear layer separation where they induce localised instabilities, thereby closing the feedback loop. This type of instability is referred to as a shear-layer (or more commonly Rossiter) mode, attributed to the early experimental work of Rossiter[17]. This led to the development of a well-known semi-empirical formula which can be used to predict a given mode frequency of oscillation for a given cavity geometry:

$$f_n = \frac{U_\infty}{L}\left(\frac{n-\alpha}{M_\infty + \frac{1}{K}}\right) \qquad \ldots (1)$$

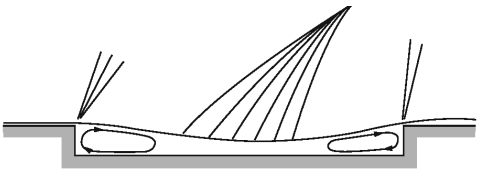
where f_n is the frequency corresponding to the nth mode, M_∞ is the freestream Mach number, K is the ratio of disturbance velocity in the shear layer to the freestream velocity, (a value of $K = 0{\cdot}57$ is widely used; although this value is appropriate for thin initial boundary layers, it decreases with increasing boundary layer thickness.) and α is an empirical constant employed to account for the phase lag between the passage of a vortical disturbance past the cavity trailing edge and the formation of an upstream travelling disturbance. The value of α depends on L/D and is evaluated as: $\alpha = 0{\cdot}062(L/D)$. Rossiter's model is generally found to agree well with experimental results at moderate subsonic Mach numbers. At transonic and supersonic Mach numbers temperature recovery within the cavity is important and hence it is essential to account for the increased sound speed within the cavity[18]. To accommodate these high Mach number ranges, Equation (1) was subsequently modified to predict the frequencies of the various oscillation modes as follows:

$$f_n = \frac{U_\infty}{L}\left(\frac{n-\alpha}{M_\infty\left[1+\frac{(\gamma-1)}{2}M_\infty^2\right]^{-\frac{1}{2}} + \frac{1}{K}}\right) \qquad \ldots (2)$$

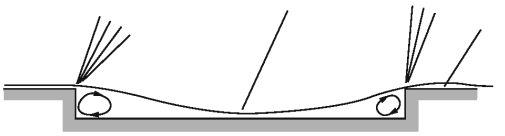
https://doi.org/10.1017/S0001924000006679 Published online by Cambridge University Press



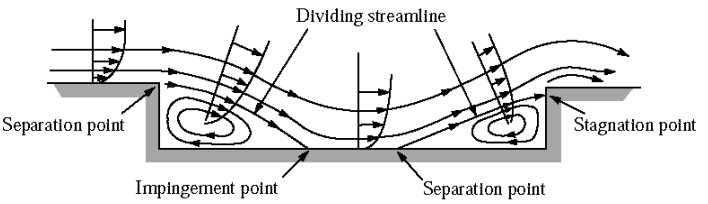
(a) open cavity flow



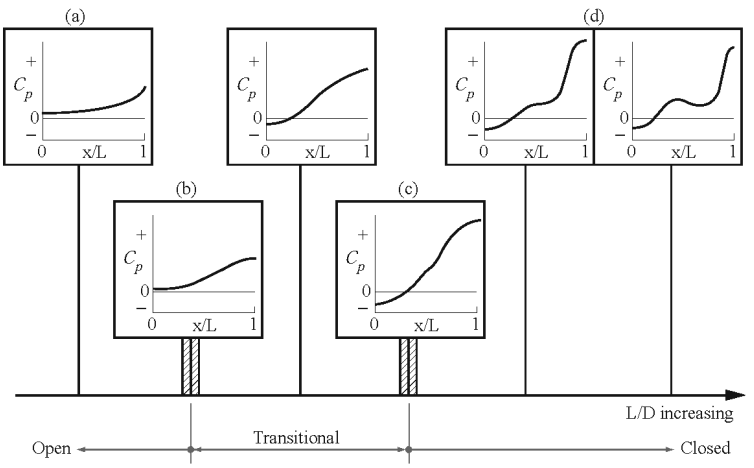
(b) transitional-open cavity flow



(c) transitional-closed cavity flow



(d) closed cavity flow



(e) cavity flow type classification, based on floor pressure distributions

Figure 2. Cavity flow types and corresponding pressure distributions[15].

https://doi.org/10.1017/S0001924000006679 Published online by Cambridge University Press

where γ is the ratio of specific heat of the test fluid (γ = 1·4 for air). The CFD results presented in this paper use Equation (2), also known as 'modified Rossiter Equation', to predict the frequencies of the various oscillation modes in cavities. This work is continuation of our effort[19] on understanding the open cavity flow behaviours and, exploring practical and effective methods to suppress the resonant modes.

2.0 COMPUTATIONAL SOLVER

The commercial CFD solver FLUENT was used to simulate all the cavity cases considered in this paper. FLUENT is a finite-volume solver and the temporal and spatial discretisation schemes available in it provide at most second-order accuracy in space and time. Options for both explicit as well as the implicit time-stepping are available with the solver. The implicit time-stepping option was used on all the simulated results presented in this paper. To model the turbulent unsteady flowfield inside the cavity, Detached-Eddy Simulation (DES) based on a one-equation model[20] was used. DES is a hybrid model which behaves as a standard SA RANS model within the attached boundary layer and as a Large-Eddy Simulation (LES) Sub-Grid Scale (SGS) model in the rest of the flow. The standard RANS SA turbulence model[20] uses the distance to the nearest wall to define a length scale d that is used to calculate the production and the dissipation terms of turbulent viscosity. In the DES formulation of the SA turbulence model[9], the length scale d is replaced with a DES length scale d_{DES} defined as:

$$d_{DES} = \min(d, C_{DES}\,\Delta) \quad \ldots (3)$$

$$\Delta = \max(\delta x, \delta y, \delta z) \quad \ldots (4)$$

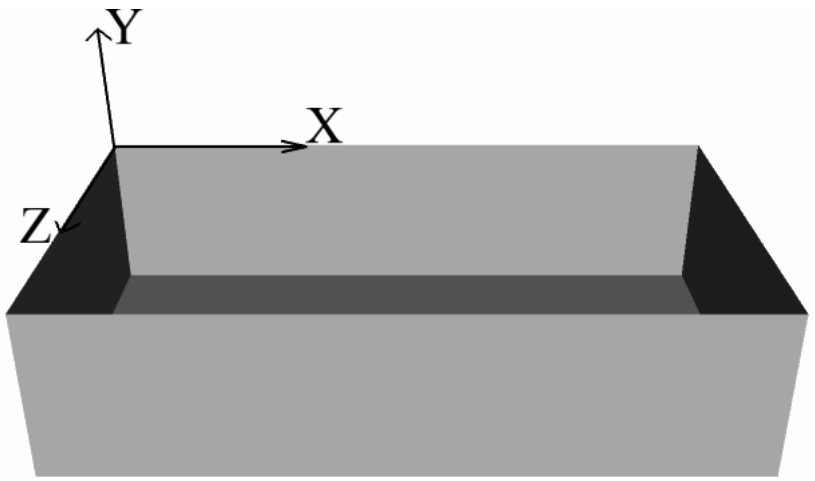
where C_{DES} is a constant with a value of 0·65 for the DES model and Δ is the largest cell dimension in the computational grid. The modified length scale calculated using the relations in Equation (3) ensures a length scale that is the same as the standard SA RANS value near the walls where $d << \Delta$ and reduces to the local grid spacing away from the walls where $d >> \Delta$. The effect of this is to activate a hybrid SA turbulence model that behaves as a standard SA RANS model within the attached boundary layers and as a LES Sub-Grid Scale model in the rest of the flow including the separated regions. From Equation (3), it can clearly be seen that this model is grid-dependent and, hence, any solution using it also relies on the grid design, i.e. depending on whether the cells in the attached boundary layer are carefully designed, a local grid spacing as the length scale will be activated rather than the standard SA RANS length scale required in the boundary layer.

3.0 GEOMETRY AND FLOW SETUP

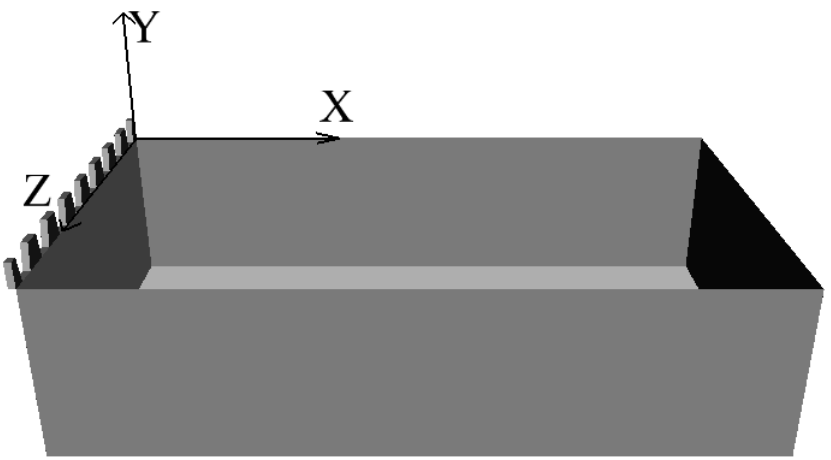
Two types of cavity geometries were considered in this investigation. Both the cavity were 10cm long with an L/D of 4 and W/D of 2·4 (see also Fig. 3) and had identical flow and geometrical settings to the experimental studies of Geraldes[21]. The first type is a three-dimensional plane cavity, which comprises a simple rectangular cutout in an otherwise infinite plate. The second type had exactly the same basic cavity dimensions as the first, the only difference being the

https://doi.org/10.1017/S0001924000006679 Published online by Cambridge University Press

presence of serrated spoilers immediately upstream of the cavity leading edge. The spoiler geometry is a slightly modified version of the coarsest (also termed as large spoiler) sawtooth spoiler used by Geraldes[21] and therefore it had identical flow conditions to the experiment. Each of the triangular elements in the experiment measured 7·375mm wide and 3·6875mm high. In this study, the spoiler geometry was modified to facilitate good quality structured grid generation in the upstream boundary layer where spoilers are located. To resolve the boundary layer correctly, structured grid cells with low skewness angles are essential and this is crucial for accurate prediction of the flowfield inside the cavity. To ensure the consistency with the experiment, the sawtooth profile was modelled as a trapezium of identical heights and surface area. The only variables were then the width of the top and the bottom parallel sides which were chosen to be 2·95mm wide and 4·425mm respectively. The spoiler profiles are shown in Fig. 4.



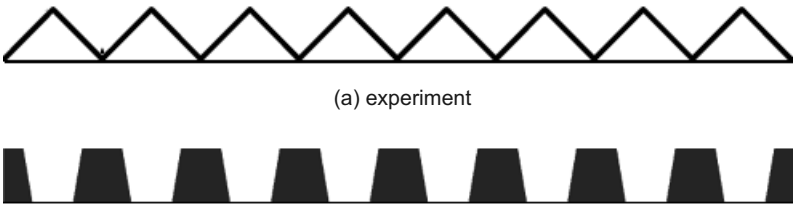
(a) clean cavity



(b) cavity with spoiler

Figure 3. Isometric views of the clean cavity and cavity with spoiler.

https://doi.org/10.1017/S0001924000006679 Published online by Cambridge University Press



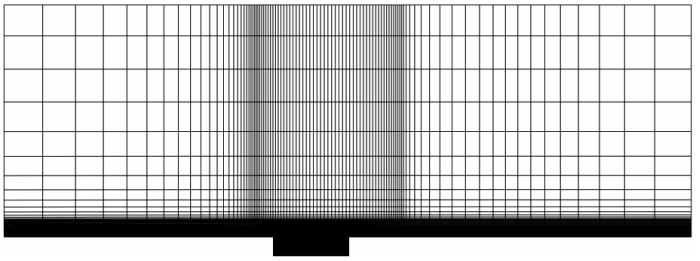
(a) experiment

(b) CFD

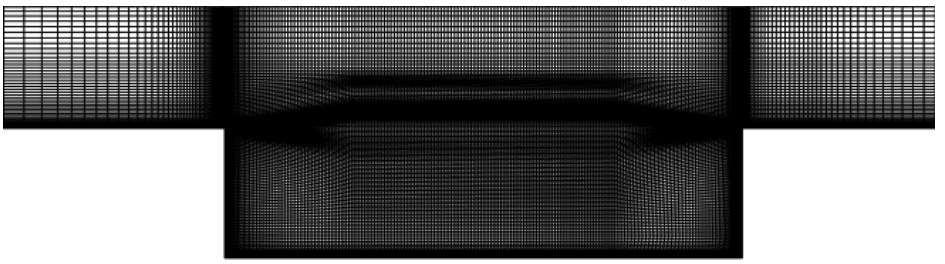
Figure 4. Spoiler geometry.

The 3D computational domains for both the cases were generated using structured meshing strategy. The non-matching grid interfacing techniques were utilised in both the computed cases to minimise the number of grids in the structured domains. The extent of the three-dimensional computational domain and mesh density were chosen following preliminary two-dimensional numerical simulations. Due to the excessive computational time involved in 3D unsteady computations, two-dimensional simulations were used to establish grid convergence. For this purpose three meshes were generated with the same basic mesh topology, but with varying grid densities. In this way, an optimum 2D grid was established. The 2D grid was chosen as the basis for the 3D grid generation. The 3D computational domain extended 4*L* upstream, 5*L* downstream and 3L vertically and laterally from the cavity walls. For the DES simulation, the 3D grid cells are ideally required to be isotropic. Hence both the cavity meshes had near isotropic cells inside the cavity with minimum stretching. Figures 5 and 6 show the sectional views of the three-dimensional computational domain for the first case (similarly, Figs 7 and 8 for the second case). The grid cells inside the cavity were maintained close to cubic volumes with a minimum amount of stretching (evident from the zoomed views in the figures) so that an LES-type length scale is invoked inside the cavity. In total, the computational domain consisted of approximately 2·6 million structured grid points for the first case (2·79 million for the second case). Along the inflow boundary, the two Cartesian velocity components *u, v* were prescribed so that the computed boundary layer just upstream of the cavity had approximately the same thickness as in the experiment[21]. The boundary-layer thickness near the cavity leading edge in the experiment was approximately 0·015m whereas with the specification of the profile upstream, the boundary-layer thickness achieved in the CFD near the cavity leading edge was 0·0101m. All the solid surfaces (cavity walls and flat plates) were treated as adiabatic walls with a no-slip condition. The rest of the boundary faces were set as pressure farfield. The lateral extents (side face) of the computational domain were at 3L from the cavity side walls so that the solution inside and around the cavity was not affected by the choice of the pressure far-field boundary conditions (Author had also tested another combination of boundary conditions (a combination of the pressure outlet, outflow and symmetry/periodic on the side faces of the domain; which showed very little effect on the flow inside the cavity compared to the pressure farfield boundary). In addition, the use of pressure farfield improved the stability of the solver (In the author's experience, the pressure farfield boundary helps the stability while using density based solvers).

https://doi.org/10.1017/S0001924000006679 Published online by Cambridge University Press

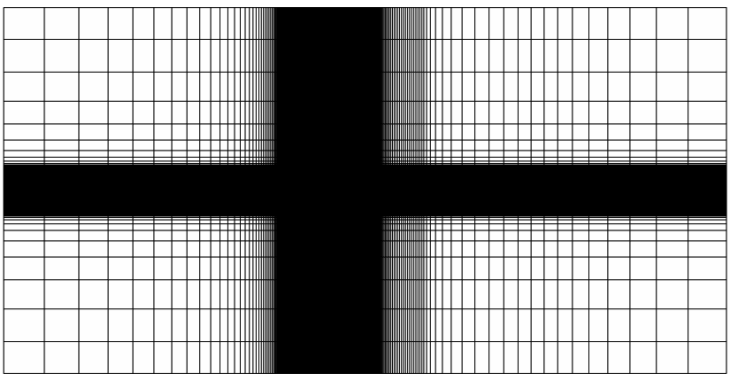


(a) section view of grid in empty cavity

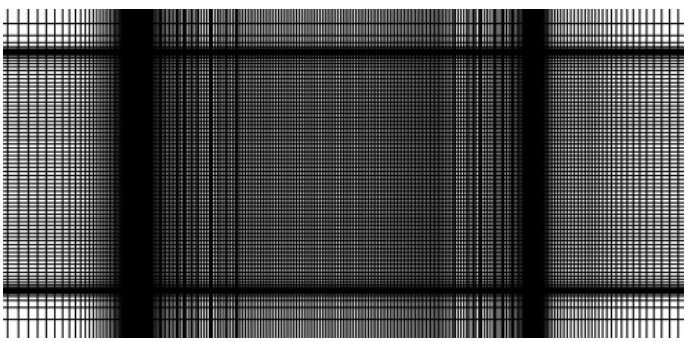


(b) section view of grid (zoomed in)

Figure 5. Structured grid distribution across *XY*-plane for clean cavity.



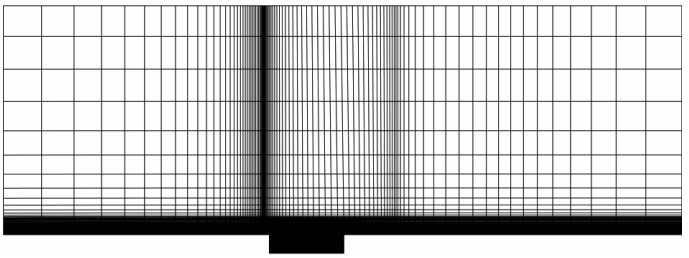
(a) section view of grid in empty cavity



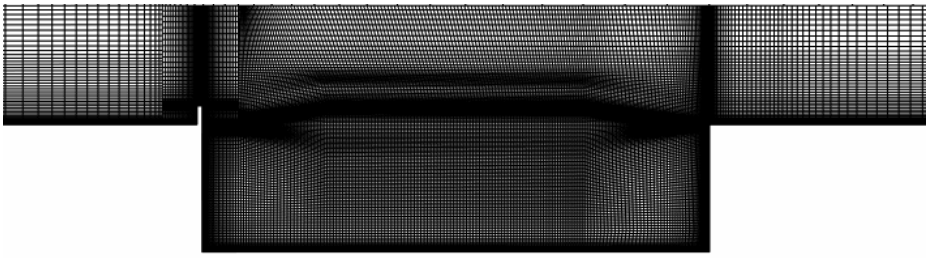
(b) section view of grid (zoomed in)

Figure 6. Structured grid distribution across *XZ*-plane for clean cavity.

https://doi.org/10.1017/S0001924000006679 Published online by Cambridge University Press

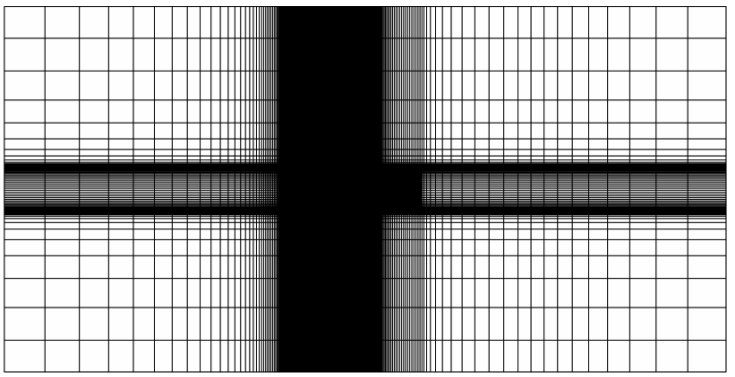


(a) section view of grid in empty cavity

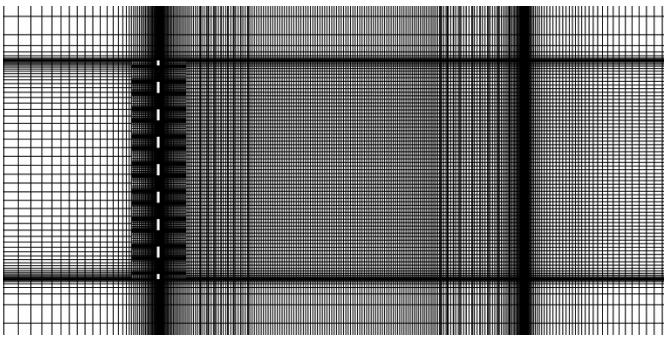


(b) section view of grid (zoomed in)

Figure 7. Structured grid distribution across *XY*-plane for cavity with spoiler.



(a) section view of grid in empty cavity



(b) section view of grid (zoomed in)

Figure 8. Structured grid distribution across *XZ*-plane for cavity with spoiler.

https://doi.org/10.1017/S0001924000006679 Published online by Cambridge University Press

4.0 COMPUTED RESULTS

The CFD solver FLUENT was used to simulate both the cavity cases considered in this paper. FLUENT is a finite-volume solver and the temporal and spatial discretisation schemes available in it provide at most second-order accuracy in space and time. Many studies[22,23] have shown FLUENT to be capable of simulating unsteady flow problems, and of resolving the flow structures responsible for noise generation when suitably designed computational mesh and time-step sizes are used. Options for both explicit as well as the implicit time-stepping are available with the solver. The spacial discretisation used in the simulations was flux difference splitting based on second order upwind (default option for compressible flow in Fluent) with a second order central differencing applied to the modified turbulent viscosity and a second order implicit scheme was adopted for temporal discretisation. Due to the transonic speed involved, a coupled solver was chosen to ensure a fully compressible solution and a constant time step (constant time-stepping is essential for the time consistency of the resolved unsteady structures especially in DES simulations) of 1×10^{-5}s (approx 2·9% of L/U_∞) was maintained for the unsteady simulation. The simulations were run initially for a total of 15,000 time steps (fully resolved unsteady flow was achieved by this time) to achieve fully resolved unsteady structures. Then the unsteady pressure monitors were activated and the flow simulations were run for further 15,000 time steps to study the spectral contents of the pressure signals at various locations in the cavity.

4.1 Plane cavity, *L/D* = 4, *W/D* = 2·4

Time-mean flow

The time-mean flowfields are characterised by their mean surface static pressure coefficient (C_p) distributions. The C_p plot for this case are presented in Fig. 9. Study of the mean C_p distribution for this case indicates that the flow belongs to the open cavity flow type and it is found to exhibit many of the same global open cavity flow behaviours. The time-mean flow within the cavity is dominated by a large-scale recirculating flow pattern. The location of the centre of the large structure may be identified from the trough in the mean C_p plot that is mostly evident along the cavity floor and the structure is centred downstream of the middle of the cavity (approximately at $x/L = 0{\cdot}58$). The computed C_p showed some discrepancies with the experiment but the global characteristics are similar. Both the CFD and experimental C_p distributions are largely flat across the floor, typical of open cavity flows.

Despite the small difference in the C_p distributions (between CFD and experiments), the internal flow structure in the cavity is largely in agreement to the experiment[21]. To analyse and understand the behaviour of the mean flow inside the cavity further, a more detailed study of the flow behaviour and structure inside the cavity using flow visualisation techniques is necessary. Hence visualisation of 2D sectional streamlines based on LIC images[24] and 3D surface flow particle tracking were used. To study 3D time-mean flow features inside the cavity, vortex core locations were calculated and stream lines were released from the calculated cores. The resulting mean flow structure is presented in Fig. 10. In addition, sectional streamlines of the computed time-mean velocity data are visualised using LIC in Fig. 11. Fig. 10 reveals the presence of two contra-rotating flow structures in the upstream third of the cavity which merge to a single, large recirculation further downstream. This is also evident from the LIC image in Fig. 11(g). These structures are described in ESDU Item 02008[15] as 'tornado-

https://doi.org/10.1017/S0001924000006679 Published online by Cambridge University Press

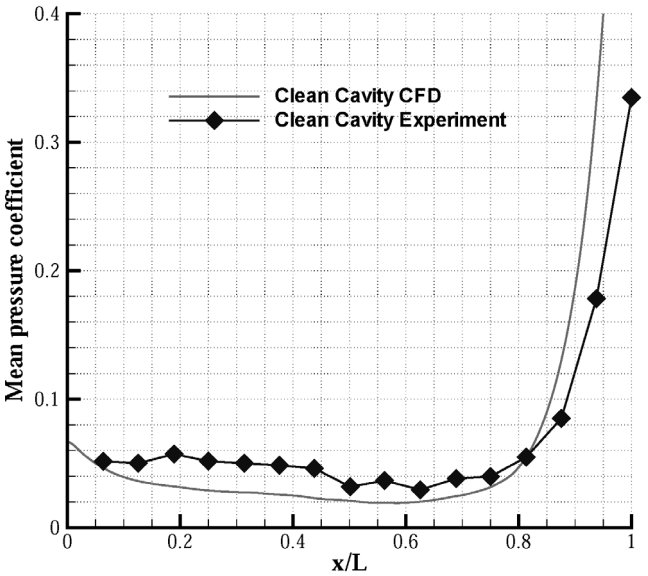


Figure 9. Centre line mean C_p along the cavity floor, L/D = 4 and W/D = 2·4.

like' vortices which spiral up towards the mouth plane (i.e. the open plane) of the cavity although speculation on their subsequent movement is not given. This has been further analysed and discussed in previous works[25,26,27], with the aid of experiments and CFD visualisation. These structures are formed when the flow travelling upstream along the floor of the cavity reaches the upstream wall. The proximity of the cavity sidewall forces the flow to divert in the spanwise direction towards the centreline of the cavity. When the flow reaches the centreline plane, it meets the flow from the other side of the centreline and is forced to turn to flow downstream but is prevented from doing so by the flow travelling upstream along the cavity floor. The flow is forced to turn out towards the sidewall of the cavity which forms the vertical 'tornado-like' structures seen on the cavity floor. Also visible in Fig. 10 are two vortices trailing downstream from the downstream corners of the cavity which is consistent with the flow visualisation works of Ref. 28. The meanflow structures captured by CFD in Figs 11(f-h) are also in good agreement with the oil flow visualisation of Ref. 28 (see Fig. 12). Hence, the global features of the mean flowfield captured by CFD agree well with the experimental observations. The LIC images of sectional streamlines at various spanwise locations (i.e. Figs 11(a-e)) also clearly indicate the three-dimensionality in the time-mean flow inside the cavity. Firstly, the most noticeable three-dimensional flow feature is the variation in the position of the core of the recirculating flow across the span of the cavity. Secondly, a secondary recirculating region exists in the upstream third of the cavity for all spanwise locations except near the centreline (z/W = 0·4 and z/W = 0·5).

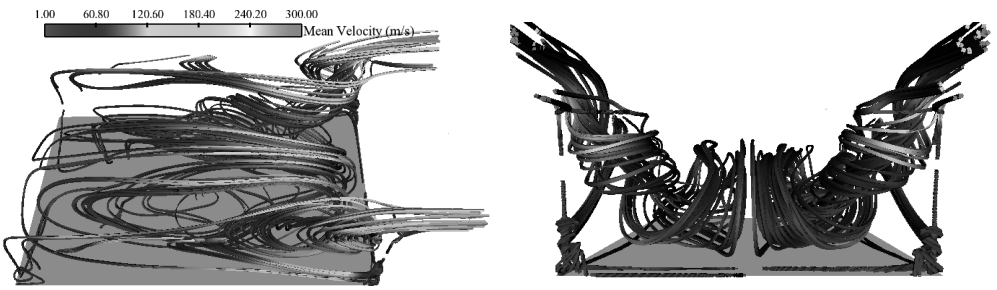
Time-dependent flowfield

The unsteady flowfield was also analysed to study the unsteady structures inside the cavity. From the result, the computed flow inside the cavity was found to be highly unsteady and dominated by periodic phenomena. The unsteady features inside the cavity and the shear layer fluctuation process may be seen in Fig. 13 which shows the time development of tubular vortical structures

https://doi.org/10.1017/S0001924000006679 Published online by Cambridge University Press

in terms of the iso-surfaces of the second invariant of the velocities[29] and their effect on the instability of shear layer. The solid red arrow represents the flow direction and the vertical arrow shows the direction of movement of the tubular structures. The presence of large-scale structures can clearly be seen from the figures. The primary effect of the 3D cavity geometry is seen to be the introduction of a warping of the vortex axis across the span of the cavity. This is partly due to the end walls retarding the growth of the vortical structures as they move downstream over the cavity. Overall, the unsteady flowfield is found to dominated by the time-dependent behaviour of the shear layer spanning the mouth of the cavity. As the incoming boundary layer separates at the cavity leading edge a shear layer is formed. As the shear layer develops downstream, convective instabilities grow leading to the formation of vortex-like structures which ultimately impinge on the downstream wall of the cavity. At the downstream end of the cavity, the interaction of the vortical structures with the cavity trailing edge generates disturbances that travel upstream along the cavity floor towards the cavity leading edge. Upon reaching the leading edge of the cavity, these tubular structures trigger instabilities in the separated shear layer completing the feedback loop. It is worth noting here that this event does not guarantee shear layer resonance. It all depends on the extent of the instability caused on the shear layer. In other words, it depends on the amount of unsteady turbulent kinetic energy the tubular structures are carrying. In Fig. 13, the amplification of initial instability on the shear layer caused by the tubular structures are monitored (marked by blue ovals). The figure shows that the shear layer instability grows quickly resulting in the violent flapping of the shear layer as it reaches the trailing edge. It will be shown later (for the same cavity geometry with vertical spoilers in the upstream boundary layer) that faintly energised structures are not able to excite strong enough instabilities on the separated shear layer to develop resonance modes.

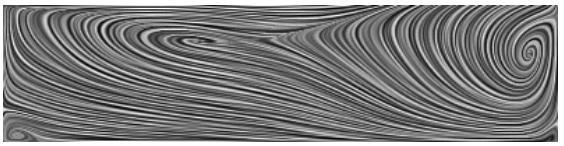
A more quantitative study of these variations may be obtained by analysing the frequency content of the nearfield pressure time-history data using fast fourier transforms. Figure 14 shows the comparison between experimental and computed pressure spectra. The data correspond to sampling points located at x/L = 0·90 on the floor of the cavity. From the comparison, the frequency of the first resonant mode is well predicted by the computation compared to experiment although the CFD under-predicts the magnitude of the tone by 4dB. Mode frequency predictions from the modified Rossiter equation are represented by the dashed lines. The computed second mode frequency (1,642Hz) however is lower than the experiment. The computed second mode frequency is found to agree better with the second mode frequency predicted by the modified Rossiter equation. Also CFD records the second mode as dominant whereas the reverse is true in the experiment. These discrepancies may be due to the lack of



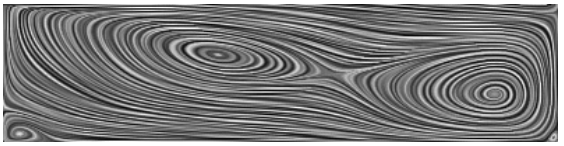
(a) 'tornado-like' vortices in the cavity (b) view from the cavity rear wall

Figure 10. Time-mean streamlines for 3D cavity, L/D = 4, W/D = 2·4 and M_∞ = 0·85.

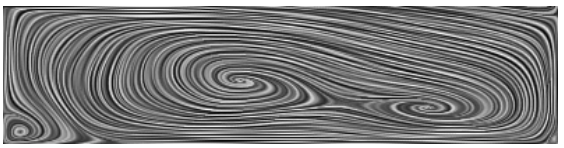
https://doi.org/10.1017/S0001924000006679 Published online by Cambridge University Press



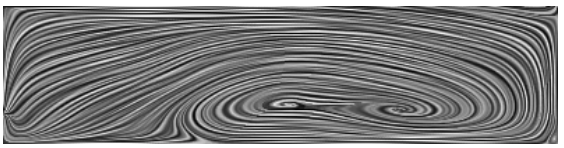
(a) time mean streamlines in x-y plane at z/W = 0·1



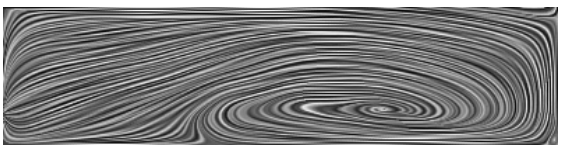
(b) time mean streamlines in x-y plane at z/W = 0·2



(c) time mean streamlines in x-y plane at z/W = 0·3



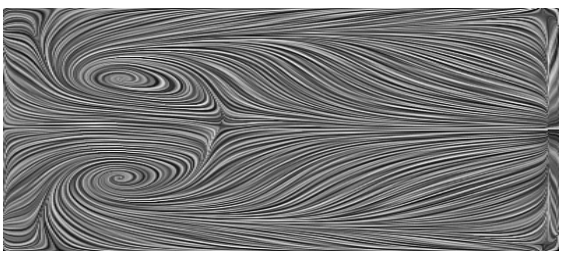
(d) time mean streamlines in x-y plane at z/W = 0·4



(e) time mean streamlines in x-y plane at z/W = 0·5



(f) upstream wall.



(g) cavity Floor



(h) downstream wall

Figure 11. Mean flow map for clean cavity using line integral convolution, L/D = 4, W/D = 2·4 and M_∞ = 0·85.

sufficient knowledge of experimental test conditions that affect the cavity flowfield e.g. incoming boundary layer characteristics, tunnel turbulence levels, ambient density (ρ) and ambient temperature (T) (or speed of sound (a_0)). Another important parameter which may have contributed to the discrepancies is the choice of turbulence model.

https://doi.org/10.1017/S0001924000006679 Published online by Cambridge University Press

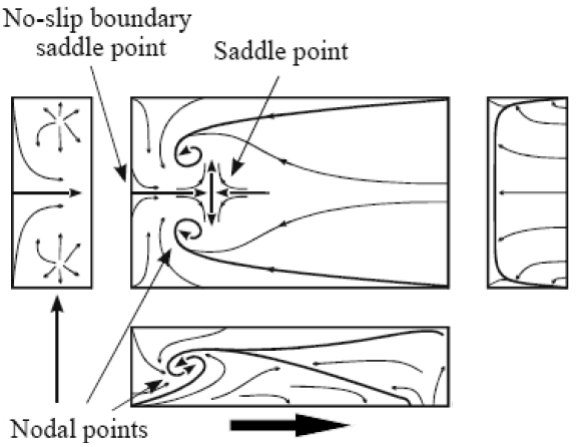


Figure 12. Oil flow visualisation for an L/D = 4 cavity[28].

4.2 Cavity with spoilers, L/D = 4, W/D = 2·4 time-mean flow

The effect of spoilers on the cavity mean flowfields are investigated first by studying the mean surface static pressure coefficient (C_p) distributions and then by mean flow visualisation. The C_p plot for this case are presented in Fig. 15 which clearly indicates the heavy pressure loss due to the presence of the spoiler. The mean C_p distribution is negative for the most of the cavity length, positive only after x/L = 0·93. The dissipation (at Kolmogorov scale) and self-regeneration of turbulent kinetic energy all takes place in the boundary layer and the presence of the spoilers act as external devices that extract energy from the flow resulting in the heavy pressure loss. To demonstrate that the non-matching grid interfaces (patch grid) is effectively used without creating any flow discontinuity and the flow structure is heavily dissipated, contours of mean Mach number are presented in Fig. 16. From the figure, it is clear that the flow is smooth across the patch interface and there is no evidence of flow structure dissipation. To analyse and understand the behaviour of the meanflow inside the cavity further, a more detailed study of the flow behaviour and structure inside the cavity was performed using flow visualisation techniques. The resulting mean flow structure is shown in Fig. 17. The meanflow streamlines do not show any evidence of spanwise flow. Also the 'tornado-like' vortices normally seen in empty cavities are absent. The 'tornado-like' vortices were described as the mean flow path of unsteady tubular structures responsible for sustaining resonance mechanisms in earlier sections. It was also highlighted (in Section 4.1) that the sustained resonant fluctuation of the shear layer was dependant on the amount of energy the vortical structures were carrying. The dissipation of turbulent kinetic energy by the spoiler meant that the structures are weakly energised and therefore are unable to sustain the spanwise flow. This also explains the absence of 'tornado- like' vortices. Also absent in Fig. 17(b) are the two vortices trailing downstream from the downstream corners of the cavity which is normally found in clean cavities. Instead uniformly spaced streamwise vortices are seen to exit from the trailing wall. This also reinforces the statement that the flow inside the cavity is unable to sustain 3D behaviour and resonant modes due to extraction of energy by the spoilers. This will be explained further while analysing unsteady results. In addition, sectional streamlines of the computed time-mean velocity data are visualised using LIC in Fig. 18. The sectional streamlines at various spanwise locations (i.e. Figs 18(b-f)) also

https://doi.org/10.1017/S0001924000006679 Published online by Cambridge University Press

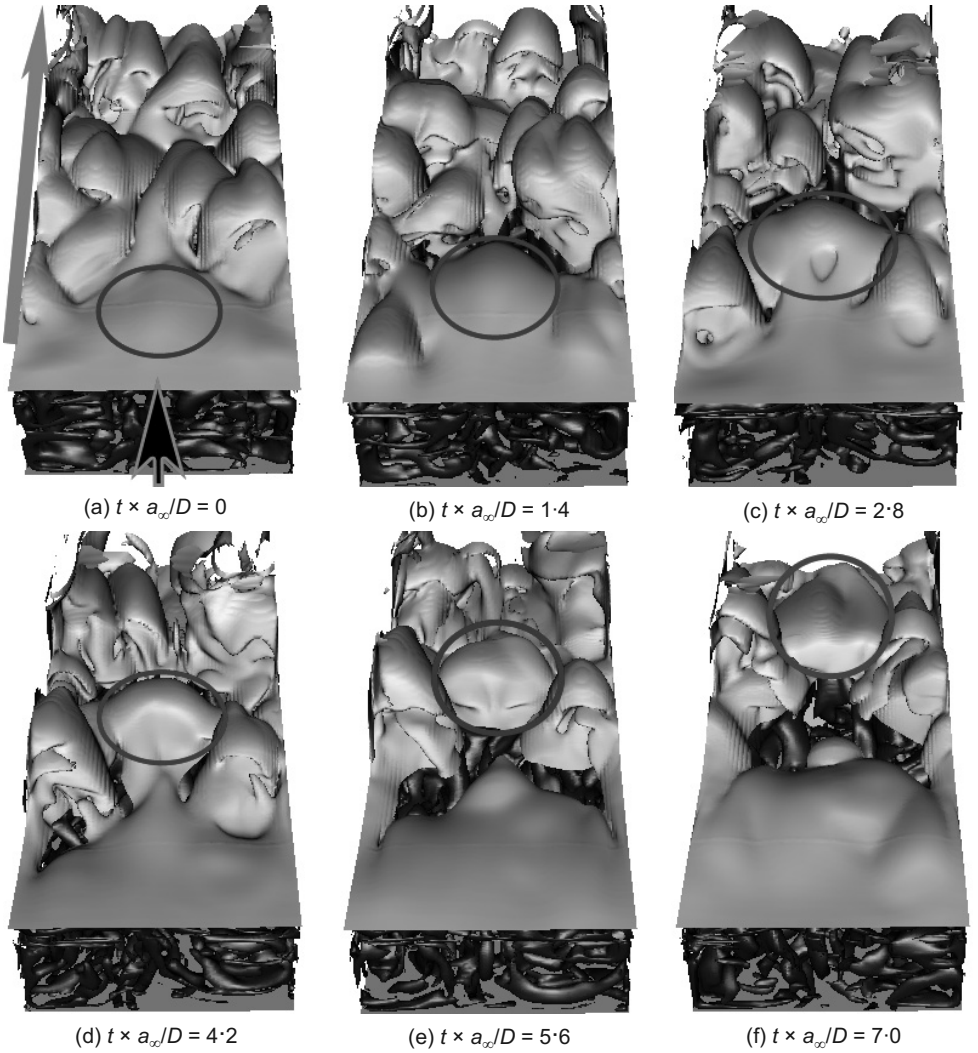


Figure 13. Shear layer vortex evolution over one cycle of oscillation: iso-contours of the Q-criterion and vorticity sheet, $L/D = 4$ and $W/D = 2{\cdot}4$; $M_\infty = 0{\cdot}85$.

indicate that the spanwise flow is not present. The position of the core of the recirculating region across the span of the cavity is approximately constant including the secondary recirculating region which exists in the upstream third of the cavity for all spanwise locations. The main feature of the mean flow pattern in the cavity floor is also consistent with the oil flow visualisation of[21] who observed a massive separation region located in the region of $x/L = 0{\cdot}25$ to $0{\cdot}3$ where all the streamlines converge (in the CFD, streamlines are seen to converge approximately at $x/L = 0{\cdot}3$).

Time-dependent flowfield

The unsteady flowfield was also analysed to study the effect of the spoilers on the unsteady flowfield inside the cavity. From the result, the computed flow inside the cavity was found to

https://doi.org/10.1017/S0001924000006679 Published online by Cambridge University Press

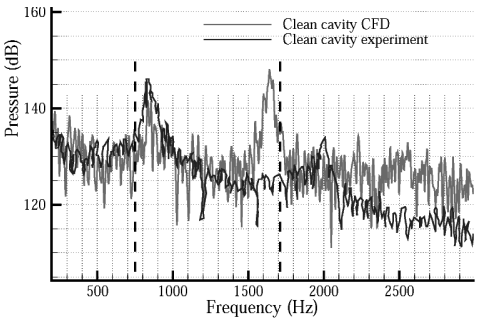


Figure 14. Pressure spectra at floor centreline, *x/L* = 0·9.

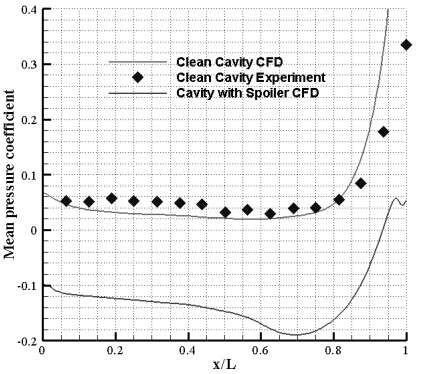


Figure 15. Centre line mean C_p along the cavity floor, *L/D* = 4 and *W/D* = 2·4.

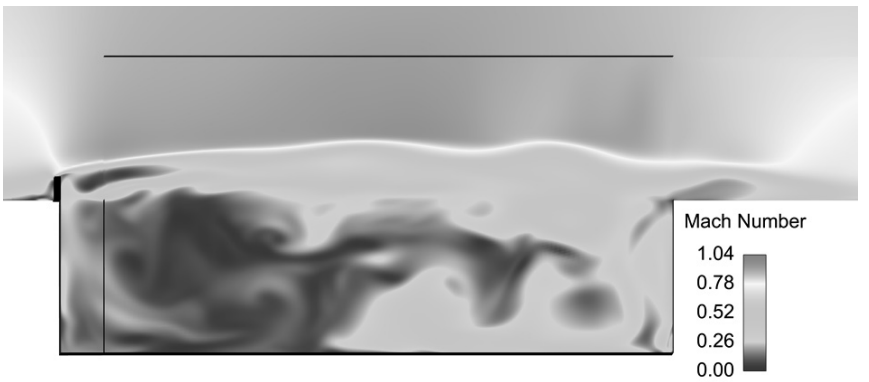
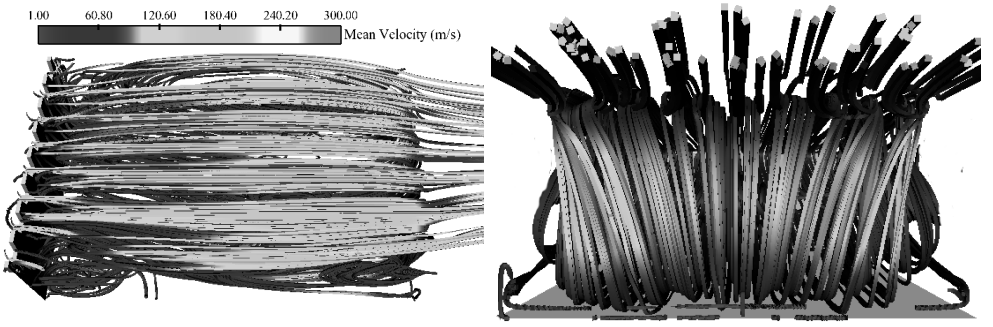


Figure 16. Instantaneous Mach number contours on XY-plane along the cavity centre line: Black lines represent the position of non-matching grid interfaces, *L/D* = 4 and *W/D* = 2·4.

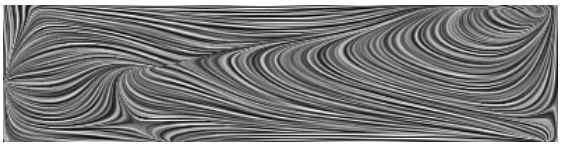


(a) streamwise streamlines without tornado vortices

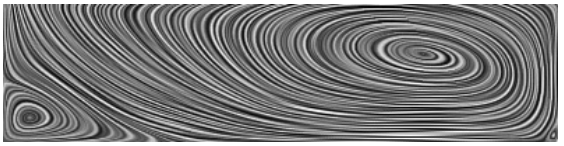
(b) view from the cavity rear wall

Figure 17. Time-mean streamlines for cavity-with-spoiler, *L/D* = 4 and *W/D* = 2·4 and M_∞ = 0·85.

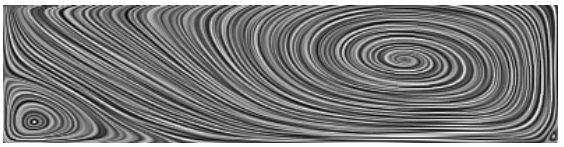
https://doi.org/10.1017/S0001924000006679 Published online by Cambridge University Press



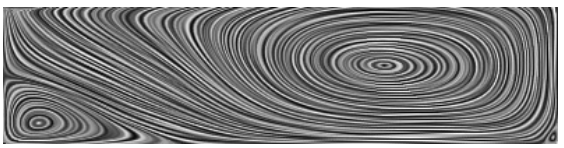
(a) time mean streamlines at side wall



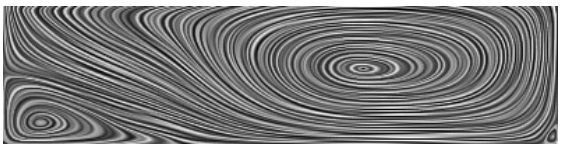
(b) time mean streamlines in x-y plane at z/W = 0·1



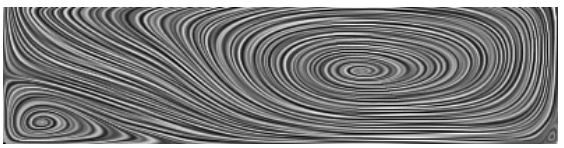
(c) time mean streamlines in x-y plane at z/W = 0·2



(d) time mean streamlines in x-y plane at z/W = 0·3



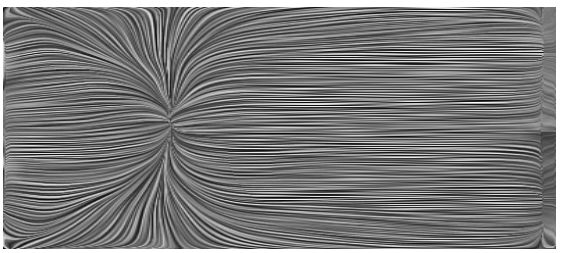
(e) time mean streamlines in x-y plane at z/W = 0·4



(f) time mean streamlines in x-y plane at z/W = 0·5



(g) upstream wall



(h) cavity Floor



(i) downstream wall

Figure 18. Mean flow map for cavity-with-spoiler using line integral convolution, L/D = 4, W/D = 2·4 and M_∞ = 0·85.

https://doi.org/10.1017/S0001924000006679 Published online by Cambridge University Press

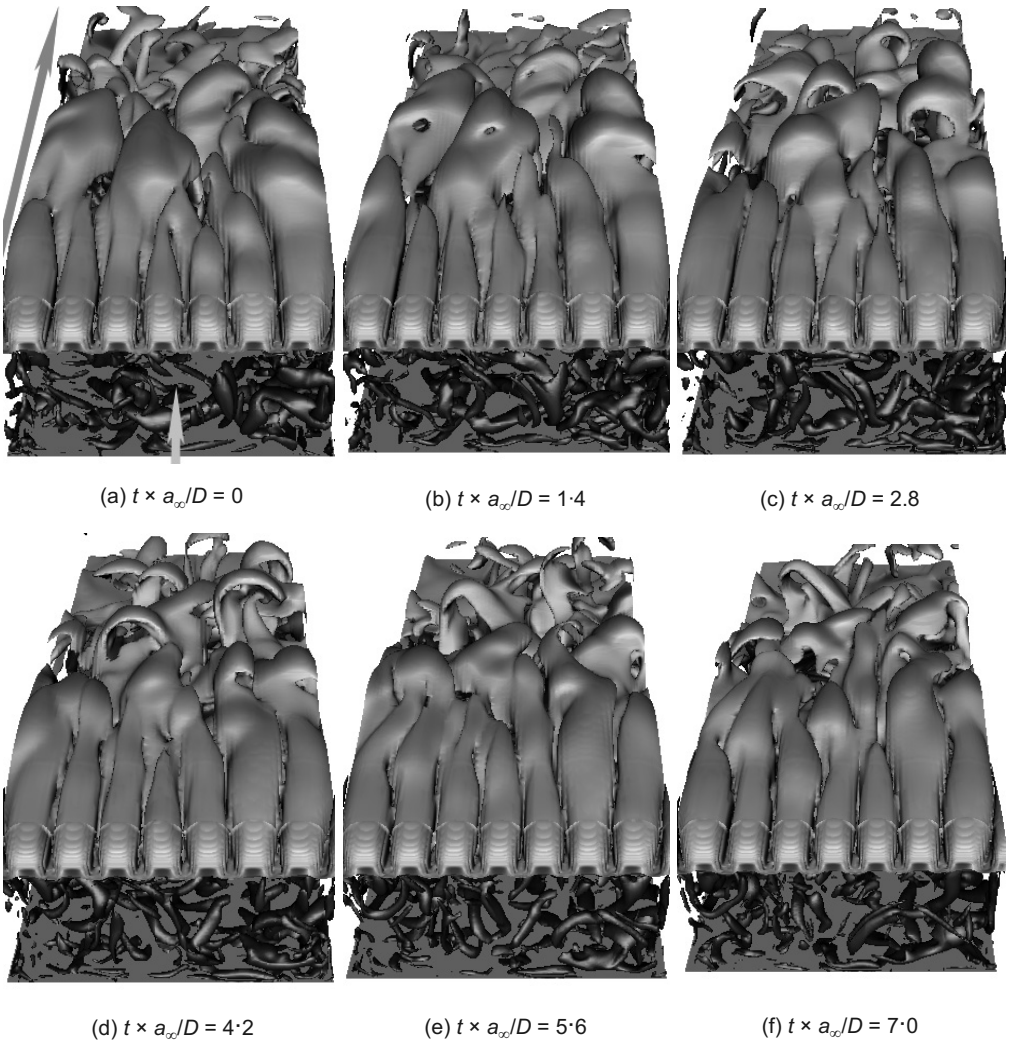


Figure 19. Shear layer vortex evolution over one cycle of oscillation: iso-contours of the Q-criterion and vorticity sheet, $L/D = 4$ and $W/D = 2{\cdot}4$; $M_\infty = 0{\cdot}85$.

be highly unsteady and dominated by periodic phenomena. The unsteady features inside the cavity and the shear layer fluctuation process may be seen in Fig. 19 which shows the time development of tubular vortical structures and their effect on the instability of the shear layer. The solid red arrow represents the flow direction and the vertical arrow shows the direction of movement of the tubular structures. The shear layer spanning the cavity width is found to be more stable in this case. To explain this, first the origin of spanwise fluctuations in the 3D clean cavity needs to be explained. The shear layer in clean cavities undergoes warping which is partly due to the slowing down of the flow by the side walls. But the main reason can be described as follows.

The wall shear stress due to the three-dimensional flat plate boundary layer upstream of the leading edge of a 3D cavity results in a component of viscous force in the spanwise direction. When the flow separates at the cavity leading edge, this spanwise force acts as an initial trigger

https://doi.org/10.1017/S0001924000006679 Published online by Cambridge University Press

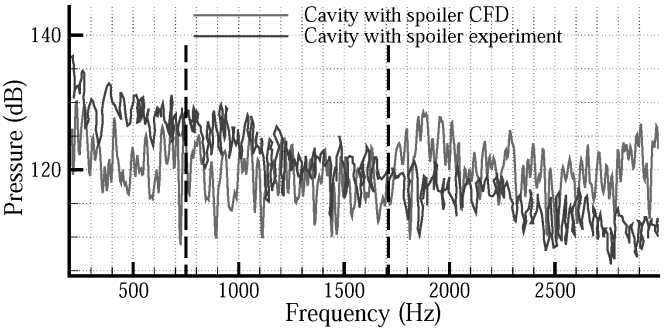


Figure 20. Pressure spectra at floor centreline, x/L = 0·9.

for the spanwise oscillation of the separated shear layer. The oscillation gets energised by the presence of unsteady turbulent energy in the flow. In the spoiler case, however, the spoilers act as a barrier against the spanwise instability. In addition, the loss of turbulent kinetic energy due to the presence of a spoiler means that the shear layer instabilities do not get enough energy to amplify. This is thought to be the reason for the stable separated shear layer. The tubular structures are seen to arrive at cavity leading edge in Fig. 19 but these structures do not have sufficient energy to cause the violent flapping of the streaks of separated shear layers. Therefore the sustained fluctuation of shear layer does not occur. In other words, the resonant modes are absent. Frequency contents of the nearfield unsteady pressure signal was extracted using fast fourier transforms for comparison with experiment. The resulting spectra is shown in Fig. 20. From the figure, the CFD result is found to record the complete suppression of the dominant tones in the presence of the spoiler consistent with the experiment. The computed broadband noise level had some discrepancies with the experiment which may be due to the lack of sufficient knowledge of the experimental test conditions that affect the cavity flowfield e.g. incoming boundary layer characteristics, tunnel turbulence levels, ambient density (ρ) and ambient temperature (T) (or speed of sound (a_0)). In overall, computed result is found to capture global characteristics well with compared to experiment.

5.0 CONCLUSION

Cavity flowfields were studied computationally at transonic speed. Mean pressure coefficients were compared for a clean cavity against experimental data and the result showed reasonably good agreement between the two. The experimental mean pressure coefficients for the cavity with spoiler case was not available, however, the computed mean C_p distribution was compared with the clean cavity case to understand the effect of the spoiler. The result indicated that the presence of spoiler results in the heavy pressure loss and this is thought to be due to the dissipation of the energy at the upstream flow resulting from the presence of the spoiler.

Analysis of the unsteady flow for the first case found that the computed frequency of the first resonant mode was in good agreement with the experiment although the CFD under-predicts the magnitude of the tone. The computed second mode frequency is lower than the experiment, however, it is found to agree better with the second mode frequency predicted by the modified Rossiter equation. Also CFD records the second mode as dominant whereas the reverse is true in the experiment. A strong oscillation feedback mechanism is found to be present within the cavity.

https://doi.org/10.1017/S0001924000006679 Published online by Cambridge University Press

The computed unsteady result for the second case showed complete suppression of resonant modes consistent with the experiment. In addition, both unsteady and meanflow visualisation techniques were used to gain significant insight into the flow physics behind the tone suppression. Based on the computed results a mechanism by which the spoiler suppresses the cavity resonant modes has been suggested. It is seen that the spoiler acts as an energy extracting device, thus, dissipating the turbulent energy from the approaching boundary layer. This then reduces the widely occurring phenomena (in empty cavities) of cross-stream warping of transverse vortical structures in the free shear layer. Unsteady flow within the cavity, therefore, has insufficient energy to excite flapping of this free shear layer to cause resonance.

REFERENCES

1. SRINIVISAN, S. and BAYSAL, O. Navier-Stokes calculations of transonic flow past cavities, *J Fluid Engineering*, September 1991, **113**, pp 369–376.
2. TAM, C.K.W. and BLOCK, P.J.W. On the tones and pressure oscillations induced by flow over rectangular cavities, *J Fluid Mechanics*, 1978, **89**, pp 373–399.
3. VAKILI, A. and GAUTHIER, C. Control of cavity flow by upstream mass-injection, *J Aircr*, February 1994, **31**, (1), pp 90–96.
4. HUANG, X. and WEAVER, D. Active control of shear layer oscillations across a cavity in the presence of pipeline acoustic resonance, *J Fluids and Structures*, March 1991, **5**, (2), pp 207–219.
5. CATTAFESTA, L., SONG, Q., WILLIAMS, D., ROWLEY, C. and ALVI, F. Active control of flow-induced cavity oscillations, *Progress in Aerospace Sciences*, 2008, **44**, (7-8), pp 479–502.
6. LAWSON, S.J. and BARAKOS, G.N. Assessment of passive flow control for transonic cavity flow using detached-eddy simulation, *J Aircr*, 2009, **46**, (3), pp 1009–1029.
7. CATTAFESTA, L., SHUKLA, D., GARG, S. and ROSS, J. Development of an adaptive weapons bay suppression system, No. AIAA–99–1901, 5th AIAA/CEAS Aeroacoustics Conference and Exhibit, Bellevue, Washington, USA, May 1999.
8. CATTAFESTA, L., WILLIAMS, D., ROWLEY, C. AND ALVI, F. Review of active control of flow-induced cavity resonance, No. AIAA–2003–3567, 33rd AIAA Fluid Dynamics Conference, Orlando, Florida, USA, June 2003.
9. SPALART, P.R. and ALLMARAS, S.R. Comments on the feasibility of LES for wings and on a hybrid RANS/LES approach, Proceedings of first AFOSR international conference on DNS/LES, Ruston, Louisiana, USA, August 1997.
10. NICHOLS, R.H. Comparison of hybrid turbulence models for a circular cylinder and a cavity, *AIAA J*, 2006, **46**, (6), pp 1207–1219.
11. SINHA, N., DASH, S., CHIDAMBARAM, N. and FINDLAY, D. A perspective on the simulation of cavity aeroacoustics, No. AIAA–1998–0286, January 1998.
12. SPALART, P.R., DECK, S., SHUR, M.L., SQUIRES, K.D., STRELETS, M.K. and TRAVIN, A. A new version of detached-eddy simulation, resistant to ambiguous grid densities, *Theoritical and Computational Fluid Dynamics*, 2006, **20**, pp 181–195.
13. XIAO, X., EDWARDS, J.R. and HASSAN, H.A. Blending functions in hybrid large–Eddy/Reynolds-averaged Navier-stokes simulations, *AIAA J*, 2004, **42**, (12), pp 2508–2515.
14. STALLINGS, R. and WILCOX, F. Experimental cavity pressure distributions at supersonic speeds, Tech. Rep. NASA–TP–2683, NASA, June 1987.
15. ESDU, Aerodynamics and aero-acoustics of rectangular planform cavities. Part I: Time-averaged flow, IHS ESDU, London, UK, 2004, ESDU Data Item 02008.
16. TRACY, M.B. and PLENTOVICH, E. Measurements of fluctuating pressure in a rectangular cavity in transonic flow at high Reynolds number, Tech. Rep. NASA–TM–4363, NASA Langley Research Center, 1992.
17. ROSSITER, J. Wind-tunnel experiments on the flow over rectangular cavities at subsonic and transonic speeds, Tech. Rep. 3438, Aeronautical Research Council Reports and Memoranda, 1966.
18. HELLER, H., HOLMES, D. and COVERT, E. Flow-induced pressure oscillations in shallow cavities, *J Sound and Vibration*, 1971, **18**, pp 545–553.
19. KHANAL, B., KNOWLES, K. and SADDINGTON, A. Computational Study of Cavity Flowfield at Transonic Speeds, No. AIAA–2009–701, 47th AIAA Aerospace Sciences Meeting, Orlando, Florida, USA, 2009.

https://doi.org/10.1017/S0001924000006679 Published online by Cambridge University Press

20. SPALART, P.R. and ALLMARAS, S.R. A one-equation turbulence model for aerodynamic flows, No. AIAA–1992–0439, 30th AIAA Aerospace Sciences Meeting and Exhibit, Reno, Nevada, USA, January 1992.
21. GERALDES, P. Instabilities in Transonic Cavity Flows, PhD thesis, Cranfield University, October 2005.
22. KIM, S., DAI, Y., KOUTSAVDIS, E.K., SOVANI, S., KADAM, N.A. and RAVURI, K.M.R. A Versatile Implementation of Acoustic Analogy Based Noise Prediction Method in a General-Purpose CFD Code, No. AIAA–2003–3202, 9th AIAA/CEAS Aeroacoustics Conference and Exhibit, Hilton Head, South Carolina, USA, May 2003.
23. MATHEY, F., MORIN, O., CARUELLE, B. and DEBATIN, K. Simulation of aeroacoustic sources in aircraft climate control systems, No. AIAA–2006–2493, 12th AIAA/CEAS Aeroacoustics Conference and Exhibit, Cambridge, Massachusetts, USA, May 2006.
24. KNOWLES, R.D., FINNIS, M.V., SADDINGTON, A.J. and KNOWLES, K. Planar visualization of vortical flows, Proceedings of IMechE Part G: *J Aerospace Engineering*, **220**, No. G6, 2006, pp 619–627, Special Issue on Integrating CFD and Experiments in Aerodynamics.
25. ATVARS, K., KNOWLES, K., RITCHIE, S.A. and LAWSON, N.J. Experimental and computational investigation of an S´ openŠ transonic cavity flow, Proceedings of the Institution of Mechanical Engineers, Part G: *J Aerospace Engineering*, 2009, **23**, (4), pp 357–368.
26. KHANAL, B., KNOWLES, K. and SADDINGTON, A.J. Computational study of flowfield characteristics due to presence of stores in cavities, 2nd CEAS European Air and Space Conference, Manchester, UK, 2009.
27. KHANAL, B., KNOWLES, K. and SADDINGTON, A.J. Study of cavity unsteady flowfield, No. ISSN0377-8312, 4th Symposium on Integrating CFD and Experiments in Aerodynamics, Belgium, 2009.
28. TABORDA, N.M., BRAY, D. and KNOWLES, K. Visualisation of three-dimensional cavity flows, No. ExHFT5, In 5th World Conference on Experimental Heat Transfer, Fluid Mechanics and Thermodynamics, Thessaloniki, Greece, 2001.
29. JOENG, J. and HUSSAIN, F. On the identification of a vortex, *J Fluid Mechanics*, **285**, 1995, pp 69–94.

https://doi.org/10.1017/S0001924000006679 Published online by Cambridge University Press